The Astrophysical Journal, 637: 400–414, 2006 January 20

INFRARED AND RADIO STUDY OF STAR-FORMING REGIONS ASSOCIATED WITH IRAS 19111+1048 AND IRAS 19110+1045

S. Vig,[1] S. K. Ghosh,[1] V. K. Kulkarni,[2] D. K. Ojha,[1] and R. P. Verma[1]

Received 2005 June 30; accepted 2005 September 27

ABSTRACT

A multiwavelength study of the star-forming regions associated with IRAS 19111+1048 and IRAS 19110+1045 has been carried out. These have been simultaneously mapped in two far-infrared bands at $\lambda_{\rm eff} = 130$ and 200 μm with $\sim 1'$ angular resolution using the TIFR 1 m balloon-borne telescope. The radio emission from the ionized gas of these regions has been imaged at 1280, 610, and 325 MHz using the Giant Metrewave Radio Telescope, India. Assuming the detected compact sources to represent exciting zero-age main sequence (ZAMS) stars, the initial mass function [$\xi(m) \propto m^{-a}$] for the IRAS 19111+1048 region is found to be quite steep, with $a = 5.3 \pm 0.5$ for the mass range $14 < m/M_{\odot} < 33$. The near-infrared (NIR) source coincident with the IRAS 19111+1048 peak is likely to be an embedded pre–main-sequence star. The spectral types of the ZAMS stars inferred independently from the radio and NIR measurements match very well for a good fraction of the radio sources having NIR counterparts. The best-fit radiative transfer models of the two IRAS sources are in good agreement with the observed spectral energy distributions. A uniform density distribution of dust and gas is implied for both the sources. The extents of ionized gas, number of ZAMS stars, presence of deeply embedded sources, and lower value of L/M for the cloud support the youth of IRAS 19110+1045 vis-à-vis its neighbor, IRAS 19111+1048, consistent with earlier studies.

Subject headings: H II regions — infrared: ISM — ISM: individual (IRAS 19110+1045, IRAS 19111+1048) — radio continuum: ISM

Online material: color figures

1. INTRODUCTION

Massive stars are born deeply embedded in dense clouds of gas and dust. An outflow phase begins during the early stage of stellar evolution. However, outflows have been more commonly seen among low-mass stars than their massive counterparts (Shepherd 2005 and references therein). This is because the evolutionary timescales of massive stars are much shorter. IRAS 19111+1048 (G45.12+0.13) and IRAS 19110+1045 (G45.07+0.13) are massive star-forming regions from which bipolar molecular outflows have been detected (Hunter et al. 1997).

The H II region IRAS 19111+1048 is well studied at many wavelengths compared to the neighboring H II region IRAS 19110+1045. Both these sources are at similar distances, and a value of 6 kpc is assumed for the present work (Simon et al. 2001; Araya et al. 2002; Fish et al. 2003). According to Matthews et al. (1977), both the *IRAS* sources belong to the same star-forming complex and are separated by $\sim 3\farcm1$. Kraemer et al. (2003) used the Mid-Infrared Array Camera 3 (MIRAC3) instrument to obtain high angular resolution ($\sim 1''$) images of the ultracompact sources associated with IRAS 19111+1048 and IRAS 19110+1045 in the mid-infrared (12.5 and 20.6 μm) as part of the Galactic Ring Survey (GRS) and resolved the IRAS 19110+1045 core into three compact sources and the IRAS 19111+1048 core into two sources. Faison et al. (1998) have presented the infrared spectroscopy (3–13 μm) of these regions and have studied the silicate and polycyclic aromatic hydrocarbon (PAH) features as well as the [Ne II] line. They have also discussed dust shell models to explain the spectral energy distributions (SEDs).

Low-resolution CO observations ($\sim 6'$ by Israel 1982; $\sim 8'$ by Sanders et al. 1986) indicate that IRAS 19111+1048 is located at the extremities of a large, clumpy molecular cloud complex with IRAS 19111+1048 lying near the center of a well-defined clump (Hoare et al. 1991). With higher angular resolution ($\sim 20''$) CO observations (using the $J = 3 \rightarrow 2$ transition), Hunter et al. (1997) found that there are several spokelike protrusions from the IRAS 19111+1048 core, unlike the IRAS 19110+1045 core.

Wood & Churchwell (1989) observed a cometary shape for IRAS 19111+1048 and a compact unresolved source for IRAS 19110+1045 from their very large array (VLA) survey at 5 and 15 GHz. High-resolution ($\sim 6''$ at 4.9 GHz and $\sim 3''$ at 8.5 GHz) radio maps of these sources have been presented by Testi et al. 1999 (hereafter TFT99). From these maps, they have extracted four compact sources from the IRAS 19111+1048 region and two from IRAS 19110+1045. Extended radio emission has been seen around both these regions. Both regions contain type I OH masers (Goss et al. 1973), but only IRAS 19110+1045 contains an H_2O maser (Genzel & Downes 1977). Similarly, it was found that methyl cyanide was detected only toward IRAS 19110+1045 and not toward the other source (Pankonin et al. 2001). The presence of massive, bipolar molecular (CO) outflows from both these sources was discovered by Hunter et al. (1997). Based on the lack of H_2O and methyl cyanide masers near the IRAS 19111+1048 core as compared to IRAS 19110+1045 as well as multiple outflows and higher CO antenna temperatures, it is believed that of the two, IRAS 19111+1048 is a more advanced site of massive star formation.

In the present paper, we carry out a comparative study of these two regions using the infrared and radio observations. A multiwavelength study of these regions has been undertaken to gain further insight into the evolutionary states of these two regions. This is accomplished using the distribution of dust and ionized gas, dust optical depths, dust temperatures, and spectral types of zero-age main sequence (ZAMS) stars in these regions. While the dust around these regions is studied using the mid- and

[1] Tata Institute of Fundamental Research, Mumbai 400 005, India.
[2] National Centre for Radio Astrophysics, Pune 411 007, India.

far-infrared emission, the ionized gas in these regions is probed using the low-frequency radio wave bands (1280, 610, and 325 MHz). The ZAMS spectral types are determined from the radio observations and near-infrared (NIR) color-magnitude diagrams. Based on the spectral types determined from the radio observations, we estimate the slope of the initial mass function (IMF) for the IRAS 19111+1048 region.

In § 2 we present the observations and other available data used for the present study. Section 3 describes the observational results. In § 4 we present the radiative transfer models for the two *IRAS* sources. A comprehensive discussion of the multiwavelength study of these two regions is carried out in § 5. Section 6 summarizes our results.

2. OBSERVATIONS AND DATA REDUCTION

2.1. *Far-Infrared Observations*

The Galactic star-forming region associated with IRAS 19111+1048 has been observed using the two-band FIR photometer system at the Cassegrain focus of the Tata Institute of Fundamental Research (TIFR) 100 cm (f/8) balloon-borne telescope. The observations were carried out during the balloon flight from the TIFR Balloon Facility, Hyderabad, in India (latitude 17°.47 north, longitude 78°.57 east) on 1998 March 8. Details of the telescope and the observational procedure are given by Ghosh et al. (1988). A pair of 2×3 composite silicon bolometer arrays, cooled to 0.3 K by liquid ^{3}He, corresponding to the two FIR bands are used to view identical parts of the sky simultaneously. The field of view of each detector is 1′.6. The in-flight parameters of the telescope optics, necessary to establish point-spread functions, etc., were determined from an optical detector array (photodiode array) in the Cassegrain focal plane of the telescope. Details of the optical instrument can be found elsewhere (Naik et al. 2000). The spectral response of each of the bands of the FIR photometer was determined in the laboratory using a Michelson interferometer and a Golay cell as a comparison detector. Hereafter, the two TIFR bands are referred to as 130 and 200 μm bands corresponding to the $\lambda_{\rm eff}$ for a modified blackbody source of temperature 25 K and a λ^{-2} emissivity law.

The regions around IRAS 19111+1048 and IRAS 19110+1045 were mapped by raster scanning the region of the sky ($\sim 30' \times 26'$) in cross-elevation with steps in elevation at the end of each scan. The sky-chopped FIR signals were gridded into a matrix with a pixel size of $0'.3 \times 0'.3$. The deconvolution of the observed signal matrix is carried out using a maximum entropy method similar to that of Gull & Daniell (1978; for details see Ghosh et al. 1988). Absolute positional accuracy of $\sim 0'.8$ (Naik et al. 2000) and angular resolution of $\sim 1'$ have been achieved in the FIR maps using this method.

2.2. *Radio Observations*

The radio continuum observations in three frequency bands, 1280, 610, and 325 MHz, were carried out using the Giant Metrewave Radio Telescope (GMRT), India. The GMRT has a Y-shaped hybrid configuration of 30 antennas, each of 45 m diameter. Six antennas are placed along the three arms (east, west, and south), and twelve antennas are located in a random but compact 1×1 km^2 pattern at the center (Swarup et al. 1991). The baselines ($\sim$100 m–25 km) provide sensitivity to large-scale diffuse emission as well as high angular resolution. The observational details are listed in Table 1.

For the observations, the primary flux density calibrators used were 3C 48 and 3C 286. Since IRAS 19111+1048 and IRAS 19110+1045 are separated by a distance of 3′.1, both lie within the primary beam of the telescope at all the frequencies. Hence, interferometric mapping with one phase center has been carried out for both the sources. The NRAO Astronomical Image Processing System (AIPS) was used for data reduction. The data were carefully checked for radio-frequency interference or other problems and suitably edited. The calibrated data are Fourier transformed and deconvolved using the IMAGR task in AIPS. Self-calibration was carried out to remove the residual effects of atmospheric and ionospheric phase corruptions and obtain the improved maps. For the lower frequency (325 and 610 MHz) images, the system temperature was obtained using the sky temperature from the 408 MHz map of Haslam et al. (1982). A correction factor equal to the ratio of the system temperature toward the source and flux calibrator has been used to scale the deconvolved images. For the sources detected (signal-to-noise ratio S/N > 10) in the radio maps, the peak positions as well as the flux densities (peak and integrated) were obtained using the task JMFITS in AIPS.

TABLE 1

Details of Radio Continuum Observations Carried out Using the GMRT, India

Parameter	Frequency Band (MHz)		
	1280	610	325
Date of observation	2001 Oct 28	2002 Jan 6	2002 Aug 30/31
Primary beam	21′.6	54′	1°.8
Synthesized beam	7″.5 × 3″.8	8″.4 × 6″.6	14″.4 × 11″.5
Position angle (deg)	−34.4	−73.8	68.4
Map noise (mJy beam^{-1})	0.8	0.7	1.3
Continuum bandwidth (MHz)	16	16	16

2.3. *Other Available Data Sets*

Other available data (2MASS, *IRAS*, *MSX*, *ISO*, and JCMT) for the regions around IRAS 19111+1048 and IRAS 19110+1045 have been used to study them at different wavelengths (1.2–850 μm). The flux densities from the images have been used for the construction of the SED in order to extract physical parameters of the star-forming regions using radiative transfer modeling (see § 4). The 2MASS point sources and images have been used to identify the sources of ionization of gas in these regions.

2.3.1. *IRAS*

The data from the *Infrared Astronomical Satellite* (*IRAS*) survey in the four bands (12, 25, 60, and 100 μm) for IRAS 19111+1048 and IRAS 19110+1045 were HIRES (High-Resolution Processing Using Maximum Correlation Method; Aumann et al. 1990) processed at the Infrared Processing and Analysis Center (IPAC, Caltech) to obtain high angular resolution maps (0′.5 × 1′.0 at 12 μm, 0′.5 × 1′.1 at 25 μm, 1′.0 × 1′.6 at 60 μm, and 1′.9 × 2′.3 at 100 μm). Apart from extracting the sources and determining the flux densities, the *IRAS*-HIRES maps at 12 and 25 μm have been used to find the spatial distribution of temperature, $T(12/25)$, and optical depth at 25 μm (τ_{25}).

IRAS 19111+1048 appears in the *IRAS* Low Resolution Spectrometer (LRS) Catalog (Olnon et al. 1986), and the spectrum of this source in the wavelength range 8–22 μm has been used for constructing the SED.

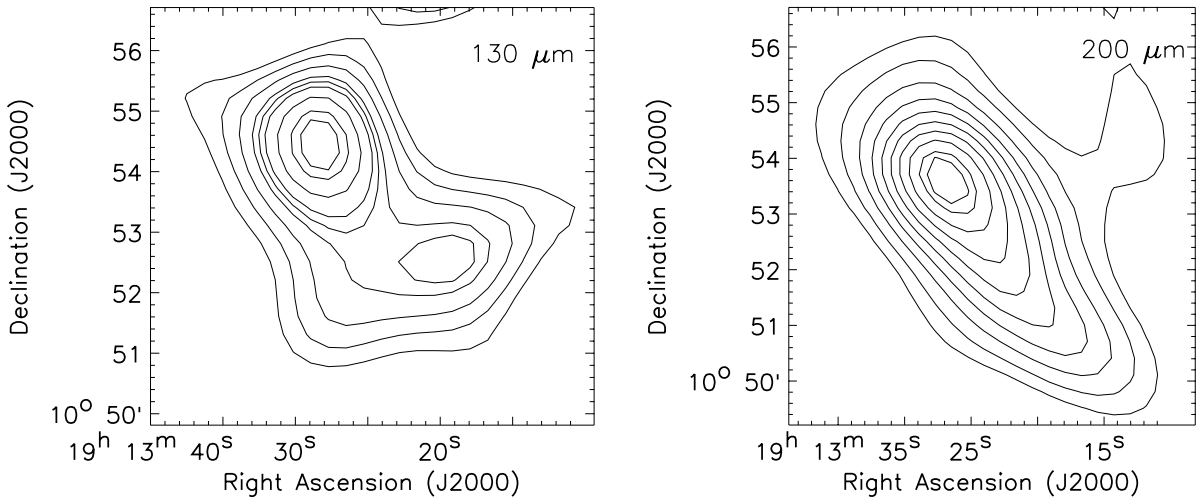

FIG. 1.—Intensity map for the region around IRAS 19111+1048, which includes IRAS 19110+1045 at 130 (*left*) and 200 μm (*right*). The effective beam size for these observations is $\sim 1'.7$. *Left*: Contour levels are at 30, 40, 50, 60, 65, 70, 80, 90, and 95 percent of the peak intensity of 620 Jy arcmin^{-2}. *Right*: Contour levels are at 12, 20, 30, 40, 50, 60, 70, 80, 90, and 95 percent of the peak intensity of 261 Jy arcmin^{-2}.

2.3.2. *MSX*

The *Midcourse Space Experiment*[3] (*MSX*) surveyed the entire Galactic plane within $|b| \leq 5^\circ$ in four mid-infrared wave bands: 8.3, 12.1, 14.7, and 21.3 μm at a spatial resolution of $\sim 18''.3$ (Price et al. 2001). The panoramic images of the Galactic plane survey of *MSX* were taken from IPAC.[4] These *MSX* maps were used to extract the sources and determine their flux densities for constructing the SED. Point sources close to these star-forming regions have been selected from *MSX* Point Source Catalog Version 2.3 (Egan et al. 2003) and cross-correlated with 2MASS sources.

2.3.3. *2MASS*

The point sources around the regions IRAS 19111+1048 and IRAS 19110+1045 were extracted from the Two Micron All Sky Survey[5] (2MASS) Point Source Catalog (PSC). The 2MASS PSC is complete down to $J \leq 15.8$, $H \leq 15.1$, and $K_s \leq 14.3$ mag for S/N > 10, in the absence of confusion. The J, H, and K_s magnitudes of the extracted sources have been used to make color-magnitude diagrams, which, in conjunction with the radio observations, are used to identify the sources responsible for ionization of gas in these regions. The JHK_s magnitudes and images were taken from IPAC.[6]

2.3.4. *ISO*

For IRAS 19110+1045, the data from the Short Wavelength Spectrometer (SWS; de Graauw et al. 1996) and the Long Wavelength Spectrometer (LWS; Clegg et al. 1996) of the *Infrared Space Observatory*[7] (*ISO*) between 2 and 188 μm have been used for constructing the SED of this source. The version of the *ISO* data used in this paper corresponds to the Highly Processed Data Product (HPDP) sets called "a uniform database of SWS 2.4–45.4 micron spectra," "high-resolution processed and defringed SWS01s," and "uniformly processed LWS L01 spectra" by Sloan et al. (2003), Frieswijk et al. (2004), and Lloyd et al. (2003), respectively, obtained from the *ISO* Data Archive.

2.3.5. *JCMT*

Submillimeter observations using the Submillimetre Common-User Bolometer Array (SCUBA) instrument of the James Clerk Maxwell Telescope[8] (JCMT) of IRAS 19111+1048 and IRAS 19110+1045 were obtained from the JCMT archive and processed using their standard pipeline, SCUBA User Reduction Facility (SURF). Maps generated at 450 and 850 μm were used to extract the sources and determine their flux densities for constructing the SEDs.

3. RESULTS

3.1. *Emission from Cold Dust*

The deconvolved TIFR far-infrared maps at the 130 and 200 μm bands are presented in Figure 1. The sources corresponding to IRAS 19111+1048 and IRAS 19110+1045 are resolved in the 130 μm map, and an extension corresponding to IRAS 19110+1045 can be seen in the 200 μm map. The flux densities of both the sources at 130 μm, and of IRAS 19111+1048 at 200 μm obtained by integrating over circular regions of diameter $3'$, centered on the far-infrared peaks, are listed in Table 2. These far-infrared wave bands probe the distribution of cold dust around this region. The color temperature of dust is obtained as $\sim$34 K for this region ($\sim 3'$) using a dust emissivity law $\epsilon_\lambda \propto \lambda^{-2}$ and assuming that the dust is optically thin.

The JCMT maps of these sources at 450 and 850 μm detect the cold dust around these regions. The distribution of the emission from dust at these wavelengths is shown in Figure 2. The maps at 450 and 850 μm correspond to beam sizes of $\sim 7'' \times 11''$ and $\sim 13'' \times 17''$, respectively.

[3] This research made use of data products from the *Midcourse Space Experiment*. Processing of the data was funded by the Ballistic Missile Defense Organization with additional support from the NASA Office of Space Science. This research has also made use of the NASA/IPAC Infrared Science Archive, which is operated by the Jet Propulsion Laboratory, Caltech, under contract with NASA.

[4] See http://irsa.ipac.caltech.edu/applications/MSX.

[5] See http://www.ipac.caltech.edu/2mass.

[6] This publication makes use of data products from the Two Micron All Sky Survey, which is a joint project of the University of Massachusetts and the Infrared Processing and Analysis Center, California Institute of Technology, funded by NASA and the NSF.

[7] Based on observations with *ISO*, an ESA project with instruments funded by ESA Member States (especially the PI countries: France, Germany, the Netherlands, and the United Kingdom) and with the participation of the Institute of Space and Astronautical Science (ISAS) and NASA.

[8] This paper makes use of data from the James Clerk Maxwell Telescope (JCMT) Archive. The JCMT is operated by the Joint Astronomy Centre on behalf of the UK Particle Physics and Astronomy Research Council, the National Research Council of Canada, and the Netherlands Organization for Pure Research.

TABLE 2
FLUX DENSITY DETAILS OF IRAS 19111+1048 AND IRAS 19110+1045

	FLUX DENSITY (Jy) FOR λ (μm)									
	TIFR IMAGES[a]		*IRAS*-HIRES IMAGES[a] *IRAS* PSC				*MSX* IMAGES[a]			
IRAS PSC SOURCE	200	130	100	60	25	12	21.3	14.7	12.1	8.3
19111+1048.....	1145	2889	6054	7024	1607	320	1411	511	316	119
			7497	5913	1395	250	...	...	...	...
19110+1045	...	2261	4409	4311	567	72.0	319	125	66	32
			<7497	<5913	494	58	...	...	...	...

[a] Fluxes obtained by integrating over a circular region of diameter 3′ centered on the peak.

3.2. *Emission from Warm Dust*

The HIRES processed maps of IRAS 19111+1048 and IRAS 19110+1045 at 12, 25, 60, and 100 μm are shown in Figure 3, where both sources are clearly resolved. Table 2 lists the flux densities determined from the HIRES maps. The *IRAS* PSC flux densities of these sources in all four wave bands are also presented for comparison.

We have used the *IRAS*-HIRES maps at 12 and 25 μm to generate the spatial distributions of dust color temperature $T(12/25)$ and optical depth at 25 μm (τ_{25}). An emissivity law of $\epsilon_\lambda \propto \lambda^{-1}$ was assumed to generate these maps. It may be noted that the spatial distribution of temperature is insensitive to the assumed value of the emissivity exponent. These wavelengths probe the warm (100–160 K) dust in the region around IRAS 19111+1048 and IRAS 19110+1045. The peak optical depth at 25 μm is 0.001, located at the peak infrared emission of IRAS 19111+1048. We have presented the distribution of τ_{25} as contours in Figure 4.

The emission in the mid-infrared from warm dust, in the *MSX* 8.3 μm band, toward these sources is shown in Figure 5 (*left*). The flux densities from the four *MSX* maps integrated for circular regions with 3′ diameter around IRAS 19111+1048 and IRAS 19110+1045 are listed in Table 2. We have modeled the thermal continuum from the interstellar dust along with the emission in the unidentified infrared bands (UIBs), using the data from *MSX* in the 8, 12, 14, and 21 μm bands, following the scheme developed by Ghosh & Ojha (2002). The peak strength of the modeled UIB emission is 5.8×10^{-4} W m^{-2} sr^{-1} at the position of IRAS 19111+1048. The spatial distribution of UIB emission resembles that of the continuum emission from warm dust at 8.3 μm. Faison et al. (1998) carried out infrared spectroscopy of central regions ($\sim$9″) of both these sources but have not detected the PAH features. The peak PAH emission obtained from *MSX* is $\sim$5 times the noise level of Faison et al. (1998). As the resolution of *MSX* is $\sim$18″, it is likely that the UIB/PAH emission has a shell-type distribution, as seen in other star-forming regions (Darbon et al. 2000). The temperature of the mid-infrared emitting dust is found

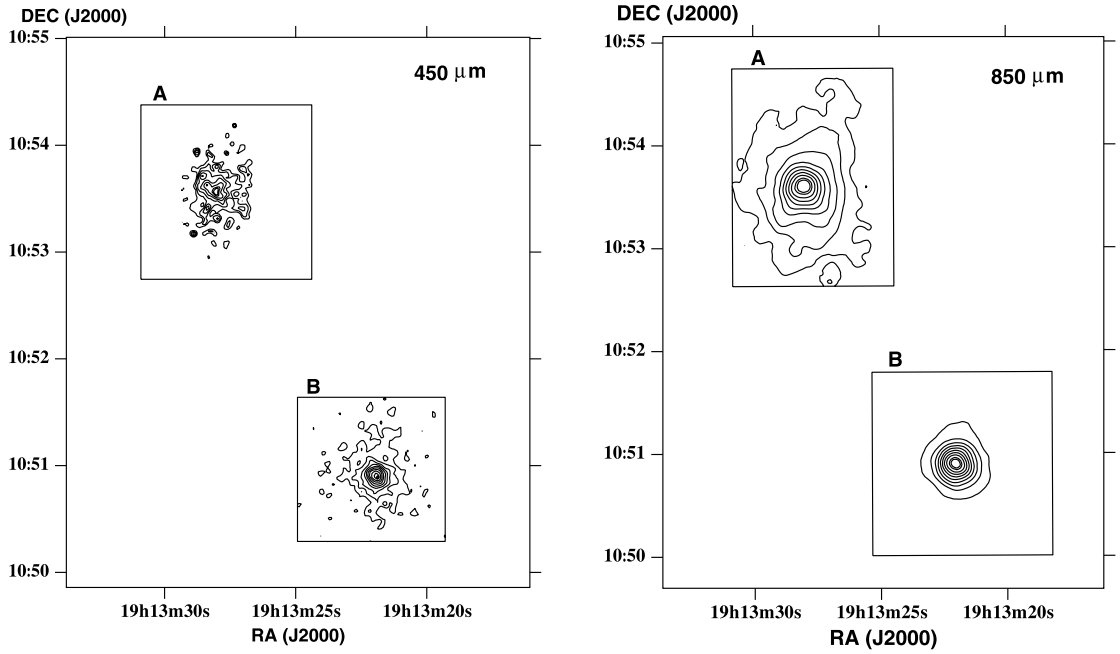

FIG. 2.—Spatial distribution of cold dust emission as obtained from JCMT at 450 (*left*) and 850 μm (*right*) around the region IRAS 19111+1048 (A) and IRAS 19110+1045 (B). The contour levels of A are at 40, 50, 60, 70, 80, 90, and 95 percent of the peak value of 25.5 Jy beam^{-1} at 450 μm and 10, 20, 30, 40, 50, 60, 70, 80, 90, and 95 percent of the peak value of 6.9 Jy beam^{-1} at 850 μm. For B, the contour levels are at 10, 20, 30, 40, 50, 60, 70, 80, 90, and 95 percent of the peak values of 161.4 and 11.0 Jy beam^{-1} at 450 and 850 μm, respectively. The maps at 450 μm (*left*) have a beam size of $\sim 7'' \times 11''$, and those at 850 μm (*right*) have a beam size of $\sim 13'' \times 17''$.

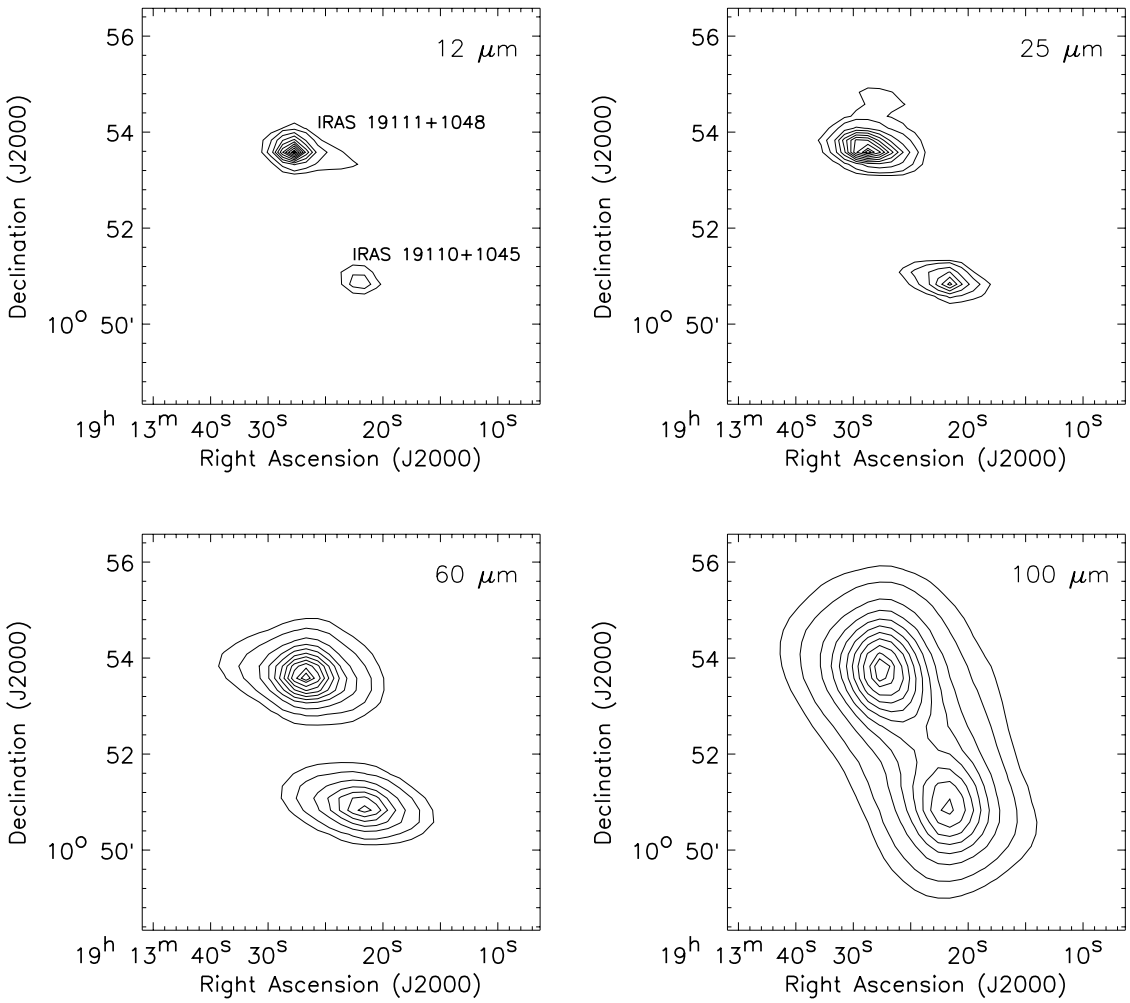

FIG. 3.—*IRAS*-HIRES intensity maps for the region covering IRAS 19111+1048 and IRAS 19110+1045 at 12 (*top left*), 25 (*top right*), 60 (*bottom left*), and 100 μm (*bottom right*). The sizes of the beams are $0'.75 \times 4'.5$ at 12 μm, $0'.75 \times 4'.6$ at 25μm, $1'.5 \times 4'.7$ at 60 μm, and $3'.0 \times 5'.0$ at 100 μm. However, the achieved angular resolutions of these HIRES maps are much higher (see text). The contours are at 5, 10, 20, 30, 40, 50, 60, 70, 80, 90, and 95 percent of the peak values of 939, 2350, 5100, and 1970 Jy arcmin^{-2} at 12, 25, 60, and 100 μm, respectively.

to be in the range 100–160 K [consistent with that obtained from *IRAS*-HIRES $T(12/25)$], the spatial distribution of which is presented as isotherms in Figure 5 (*right*).

3.3. *Emission from Ionized Gas*

The radio continuum emission from the regions around IRAS 19111+1048 and IRAS 19110+1045 at 1280 MHz is shown in Figures 6 and 7, respectively. The corresponding maps at 610 and 325 MHz are shown in Figures 8 and 9, respectively. The synthesized beam sizes and the rms noise in the maps are given in Table 1. As can be seen from the radio emission maps at 1280 MHz, 20 discrete sources have been detected in the region around IRAS 19111+1048, and seven in the IRAS 19110+1045 region (with S/N > 10). A list of these sources along with their peak and integrated flux densities at 1280 and 610 MHz is presented in Tables 3 and 4. We designate these sources as S1, S2, . . . , S27. The total integrated flux densities for IRAS 19111+1048 at 1280, 610, and 325 MHz are 6.60 ± 0.01, 3.90 ± 0.01, and 0.8 ± 0.02 Jy, respectively. The extent of ionized gas of the H II region IRAS 19111+1048 is $\sim$2.8 pc, while that of IRAS 19110+1045 is $\sim$1.3 pc. The flux density measurement of IRAS 19111+1048 was carried out by Altenhoff et al. (1979) at 4.875 GHz with the Effelsberg 100 m telescope (beam $\sim 2'.6$). Scaling this measurement to 1.280 GHz under the assumption that it is optically thin at both these frequencies, we find that with the interferometer, we have collected $\sim$95% of the total flux density measured with the single dish, demonstrating that almost all structural features have been captured by the baselines of GMRT. For IRAS 19110+1045, the total integrated flux densities are 730 ± 6, 552 ± 6, and 110 ± 4.3 mJy at 1280, 610, and 325 MHz, respectively.

Assuming that each discrete source in the radio continuum maps represents an exciting ZAMS star, the spectral types of the sources have been estimated using the integrated flux densities from our GMRT maps and the formulation of Schraml & Mezger (1969) and Panagia (1973). The ZAMS spectral types determined in this way are listed in Tables 5 and 6. As can be seen, all the sources are earlier than B0.5. For the sources also detected by TFT99, we have compared the spectral types obtained from our GMRT maps as well as from the flux densities given by TFT99b and these are found to be consistent (see Tables 5 and 6).

3.3.1. *Physical Properties of the Compact Cores*

The physical properties such as the electron temperature and emission measure of the compact core of IRAS 19111+1048 (shown as "14" in Fig. 6 and S14 in Table 3) can be estimated using the flux densities of the unresolved core at low frequencies (1280 and 610 MHz from the GMRT images) as well as at higher frequencies (4.9 and 8.5 GHz using the listed parameters of this

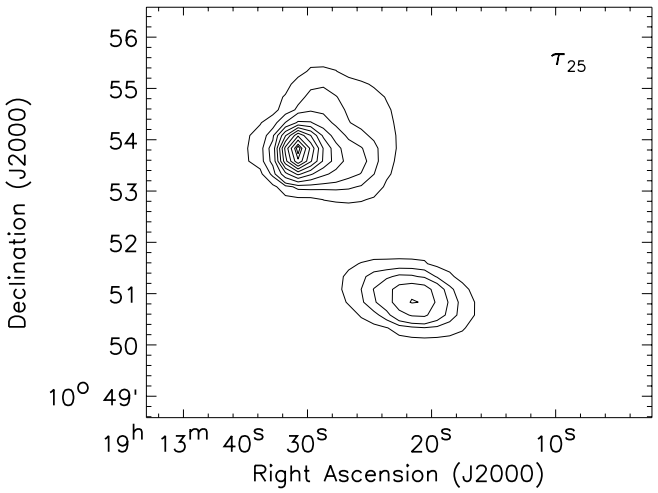

FIG. 4.—Distribution of optical depth at 25 μm, τ_{25}, of the region around IRAS 19111+1048 and IRAS 19110+1045 assuming a dust emissivity law of $\epsilon_\lambda \propto \lambda^{-1}$. The τ_{25} contours represent 1, 5, 10, 20, 30, 40, 50, 60, 70, 80, and 90 percent of the peak value of 0.001.

core from Table 1 of TFT99). Under the approximation that the core is homogeneous and spherically symmetric, the flux density S (Mezger & Henderson 1967) is given by

$$S = 3.07 \times 10^{-2} T_e \nu^2 \Omega (1 - e^{-\tau(\nu)}),$$

$$\tau(\nu) = 1.643 \times 10^5 a \nu^{-2.1} (\mathrm{EM}) T_e^{-1.35},$$

where S is the integrated flux density in Jy, T_e is electron temperature in K, ν is the frequency in MHz, τ is the optical depth, Ω is the solid angle subtended by the source in steradians (which in this case is the synthesized beam size for the unresolved core), and EM is the emission measure in cm^{-6} pc. The factor a represents the deviation between the exact formulation and its approximation. We use $a = 0.99$, obtained from Table 6 of Mezger & Henderson (1967), for the frequency range 0.6–

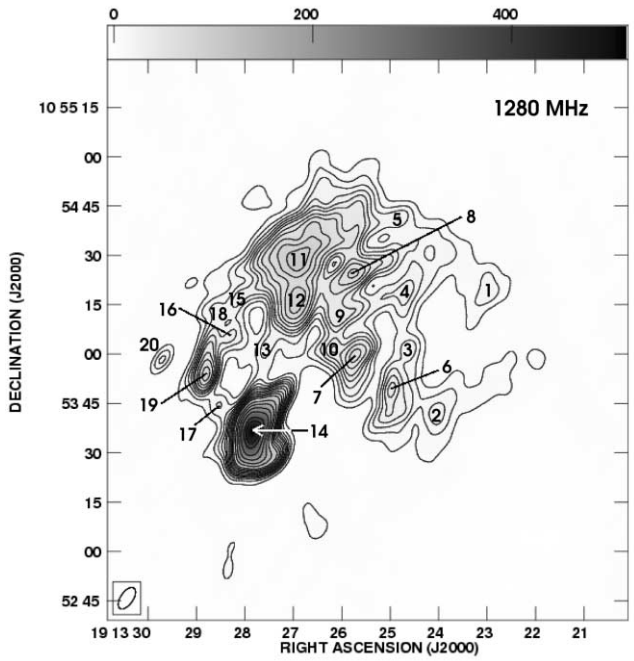

FIG. 6.—Radio continuum emission at 1280 MHz from IRAS 19111+1048. The contour levels are at $3.0 \times (-2, 2, 4, 6, 8, 10, 12, 15, 18, 22, 26, 31, 42, 54, 70, 90, 120, 140)$ mJy beam^{-1}. The beam size is $7\farcs5 \times 3\farcs8$, and the rms noise in the map is $\sim$0.8 mJy beam^{-1}. The discrete radio sources are represented by the numbers as listed in Tables 3 and 5.

8 GHz for $T = 10{,}000$ K. The peak flux densities of the cores after convolving the images to a common resolution ($10'' \times 10''$) have been used to fit the above equations using the nonlinear least-squares Marquardt-Levenberg algorithm. The observed and the best-fit model flux densities are shown in Figure 10. For the best-fit model, the electron temperature and emission measure (with 1 σ errors) of the IRAS 19111+1048 core are 8346 $\pm$ 1511 K and 8.8 $\pm$ 0.7 $\times$ 10^6 cm^{-6} pc, respectively. Wood & Churchwell (1989) used the H76α recombination line to obtain the electron temperature of 7900 $\pm$ 1000 K, which is consistent with our value

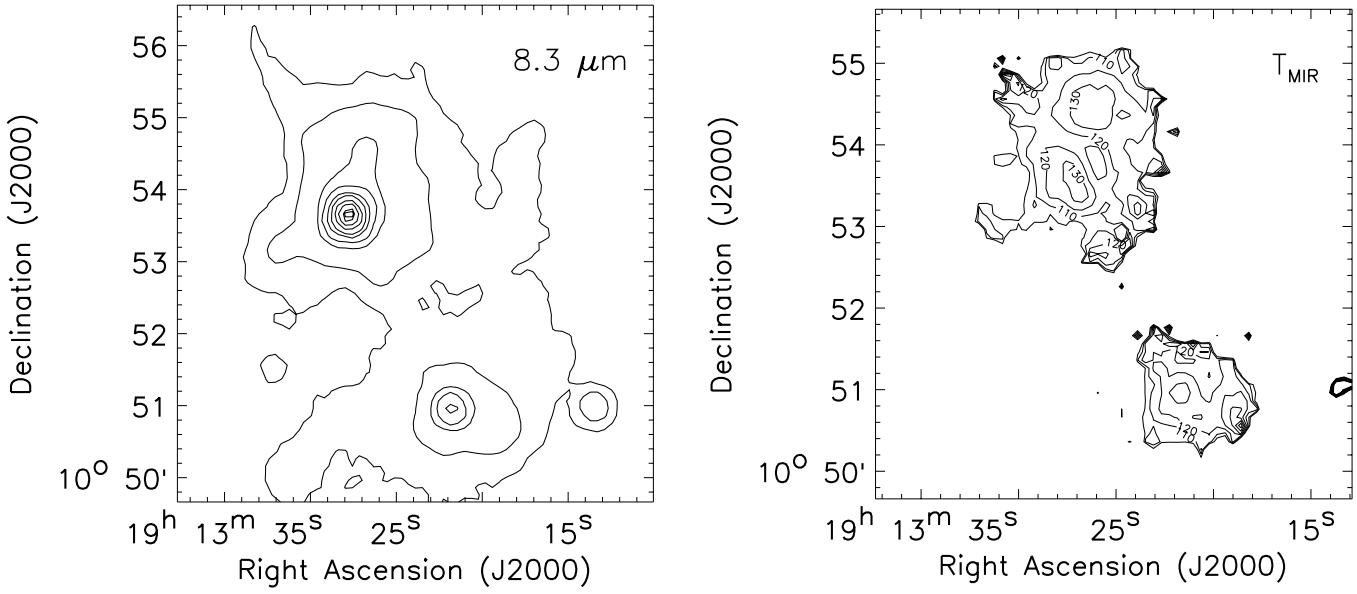

FIG. 5.—Spatial distribution of continuum emission in the *MSX* 8.3 μm band (*left*) with a beam of $\sim$18$''$ and mid-infrared temperature T_{MIR} (*right*). The contour levels are at 0.5, 1, 5, 10, 20, 30, 50, 70, 90, and 95 percent of peak value of 473.7 Jy arcmin^{-2} (*left*) and at 100, 110, 120, 130, 140, 150, and 160 K (*right*).

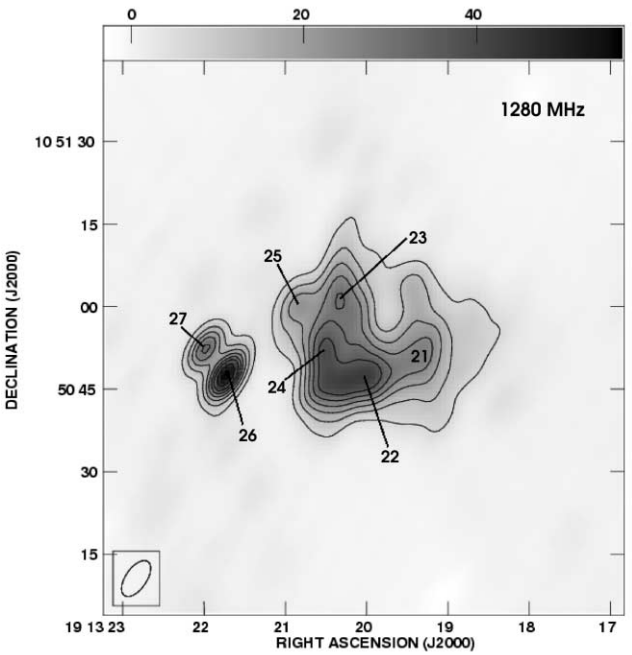

FIG. 7.—Radio continuum emission at 1280 MHz from IRAS 19110+1045. The contour levels are at $3.0 \times (-2, 2, 4, 6, 8, 10, 12, 14, 16, 18)$ mJy beam^{-1}. The beam size is $7\farcs5 \times 3\farcs8$, and the rms noise in the map is $\sim$0.8 mJy beam^{-1}. The discrete radio sources are represented by the numbers as listed in Tables 4 and 6.

within the errors. Using radio continuum emission at 15 GHz, they obtained the peak ($0\farcs4 \times 0\farcs4$) values of the electron temperature and emission measure as 8100 K and 1.5×10^9 cm^{-6} pc, respectively. The difference in EM values could be due to a clumpy distribution of ionized gas. Lumsden & Puxley (1996) obtained an electron temperature of 8000–9000 K by means of a best fit to the near-infrared spectrum of the IRAS 19111+1048 core.

The compact cores S26 and S27 belonging to the IRAS 19110+1045 region are resolved at 1280 MHz but not at 610 MHz. They are, however, resolved in the 4.9 and 8.5 GHz maps of TFT99. While S26 appears to be optically thin at these three frequencies (1280 MHz, 4.9 GHz, and 8.5 GHz), S27 appears to be optically thick. For an assumed temperature of 8000 K, the best-fit emission measure for S26 is $(2.5 \pm 0.3) \times 10^5$ cm^{-6} pc. Since S27 is a compact unresolved source at all these three frequencies, we estimate the size of S27 to be 0.026 pc using the flux density at 1280 MHz for a similar temperature. Assuming a photon-bounded uniform-density region, this size implies an electron density $n_e = 1.5 \times 10^4$ cm^{-3}. Garay et al. (1986) modeled this source as an ionized toroid of size 0.03 pc (scaled to our distance) and obtained $n_e = 1.6 \times 10^5$ cm^{-3}, which are comparable.

3.4. *Embedded Star Cluster*

With the aim of identifying early-type stars in the embedded cluster of the two H II regions, we study the NIR point sources from the 2MASS PSC in the J, H, and K_s bands. In this section, we discuss the nature of these sources. We have used the color-magnitude (CM) diagrams of the sources in the regions around IRAS 19111+1048 and IRAS 19110+1045 to estimate the spectral types of the stars. For IRAS 19111+1048, 47 stars were found in a circle of radius $1\farcm2$ around the center of the radio emission ($\alpha_{2000} = 19^h13^m26\fs0$, $\delta_{2000} = +10^\circ54'11''$) that were detected in all the three JHK_s bands of 2MASS. All the sources whose magnitudes are given as upper limits have been excluded from the study. A similar study was carried out for the source IRAS 19110+1045. Within a circle of radius $1'$ around this source ($\alpha_{2000} = 19^h13^m20\fs6$, $\delta_{2000} = +10^\circ50'47''$), 42 stars were detected in all the three 2MASS bands. A list of the positions and apparent magnitudes of the 2MASS sources that are likely to be associated with

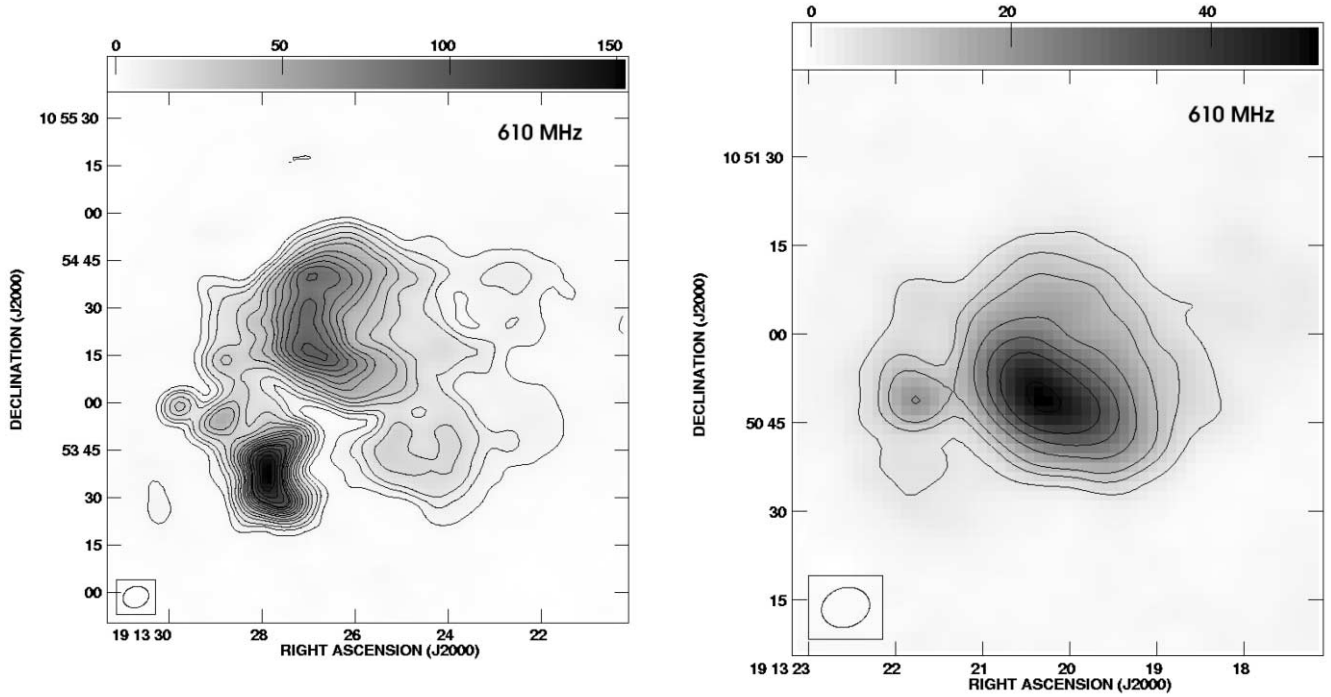

FIG. 8.—Radio continuum emission at 610 MHz from IRAS 19111+1048 (*left*) and IRAS 19110+1045 (*right*). The contour levels are at $2.0 \times (-2, 2, 4, 6, 10, 14, 18, 24, 28, 33, 38, 43, 47, 49, 55, 61, 68, 75, 82)$ mJy beam^{-1} (*left*) and at $2.0 \times (-2, 2, 4, 6, 10, 14, 18, 24)$ mJy beam^{-1} (*right*). The beam size is $8\farcs2 \times 6\farcs6$, and the rms noise in the map is $\sim$0.7 mJy beam^{-1}.

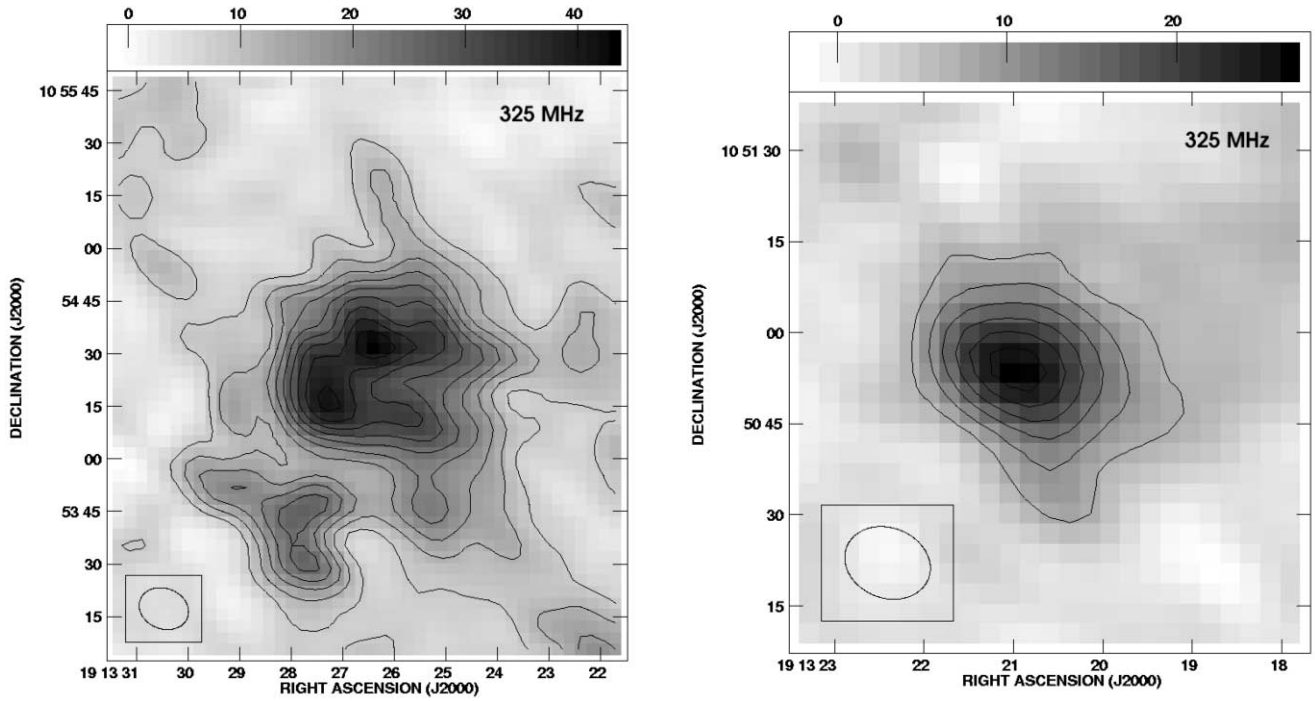

FIG. 9.—Radio continuum emission at 325 MHz from IRAS 19111+1048 (*left*) and IRAS 19110+1045 (*right*). The contour levels are at $4.0 \times (-2, 2, 3, 4, 5, 6, 7, 8, 9, 10)$ mJy beam^{-1} (*left*) and at $3.5 \times (-2, 2, 3, 4, 5, 6, 7)$ mJy beam^{-1} (*right*). The beam size is $14\farcs5 \times 11\farcs4$, and the map noise is $\sim$1.3 mJy beam^{-1}.

TABLE 3

EXTRACTED SOURCES AND THEIR FLUX DENSITIES FROM RADIO MAPS OF IRAS 19111+1048

			1280 MHz		610 MHz	
SOURCE NO.	R.A. (J2000.0)	DECL. (J2000.0)	Peak Flux (mJy beam^{-1})	Int. Flux (mJy)	Peak Flux (mJy beam^{-1})	Int. flux (mJy)
S1	19 13 23.0	+10 54 20	16.5 ± 0.5	77.0 ± 2.7	...	...
S2	19 13 24.0	+10 53 42	20.5 ± 0.5	117.5 ± 3.5	...	...
S3	19 13 24.7	+10 54 01	22.4 ± 0.5	81.5 ± 2.4	...	...
S4	19 13 24.7	+10 54 19	28.0 ± 0.5	169.2 ± 3.7	19.6 ± 0.7	115.2 ± 5.2
S5	19 13 24.9	+10 54 41	23.5 ± 0.5	90.2 ± 2.2	...	...
S6	19 13 24.9	+10 53 48	34.5 ± 0.5	325.5 ± 5.5	22.5 ± 0.6	313.6 ± 7.5
S7	19 13 25.7	+10 54 00	56.4 ± 0.5	256.7 ± 2.9	25.6 ± 0.7	221.8 ± 9.2
S8	19 13 25.8	+10 54 24	67.3 ± 0.5	328.1 ± 3.0	...	...
S9	19 13 26.1	+10 54 12	44.8 ± 0.5	247.1 ± 3.4	...	...
S10	19 13 26.1	+10 54 02	37.4 ± 0.5	157.3 ± 2.7	...	...
S11	19 13 26.9	+10 54 29	101.3 ± 0.5	1261.7 ± 6.3	...	...
S12	19 13 26.9	+10 54 17	88.3 ± 0.5	669.6 ± 4.5	...	...
S13	19 13 27.5	+10 54 03	21.7 ± 0.5	103.7 ± 3.0	...	...
S14	19 13 27.8	+10 53 36	487.8 ± 0.5	2156.6 ± 2.8	150.7 ± 0.8	833.7 ± 5.1
S15	19 13 28.1	+10 54 18	27.9 ± 0.5	136.3 ± 3.0	...	...
S16	19 13 28.4	+10 54 06	26.3 ± 0.5	97.9 ± 2.5	...	...
S17	19 13 28.5	+10 53 44	18.1 ± 0.5	53.7 ± 2.1	...	...
S18	19 13 28.7	+10 54 13	20.0 ± 0.5	97.4 ± 2.9	30.0 ± 0.8	89.3 ± 3.0
S19	19 13 28.8	+10 53 55	72.4 ± 0.5	178.7 ± 2.0	43.5 ± 0.8	154.7 ± 3.5
S20[a]	19 13 29.7	+10 53 58	20.0 ± 0.5	21.1 ± 1.0	29.4 ± 0.9	30.6 ± 1.6

NOTE.—Units of right ascension are hours, minutes, and seconds, and units of declination are degrees, arcminutes, and arcseconds.

[a] Nonthermal source.

TABLE 4
Extracted Sources and Their Flux Densities from Radio Map of IRAS 19110+1045

Source No.	R.A. (J2000.0)	Decl. (J2000.0)	1280 MHz Peak Flux (mJy beam^{-1})	1280 MHz Int. Flux (mJy)	610 MHz Peak Flux (mJy beam^{-1})	610 MHz Int. Flux (mJy)
S21	19 13 19.4	+10 50 51	27.1 ± 0.6	124.1 ± 2.2	...	426.1 ± 4.0[a]
S22	19 13 20.1	+10 50 48	45.9 ± 0.6	183.3 ± 2.2	...	426.1 ± 4.0[a]
S23	19 13 20.3	+10 50 59	32.4 ± 0.6	87.5 ± 1.8	...	426.1 ± 4.0[a]
S24	19 13 20.4	+10 50 49	42.9 ± 0.4	81.9 ± 1.4	...	426.1 ± 4.0[a]
S25	19 13 20.8	+10 50 59	23.2 ± 0.6	28.0 ± 1.0	...	426.1 ± 4.0[a]
S26	19 13 21.7	+10 50 48	56.0 ± 0.6	69.5 ± 1.3	...	34.9 ± 1.3[b]
S27	19 13 22.0	+10 50 52	30.6 ± 0.6	44.5 ± 1.4	...	34.9 ± 1.3[b]

Note.—Units of right ascension are hours, minutes, and seconds, and units of declination are degrees, arcminutes, and arcseconds.
[a] Same value of integral flux density is given as S21–S25 are unresolved.
[b] Same value of integral flux density is given as S26 and S27 are unresolved.

the radio sources of the IRAS 19111+1048 and IRAS 19110+1045 regions (see § 5) is presented in Table 7. The CM diagrams ($J - H$ vs. J) for the sources detected in the 2MASS JHK_s bands around the IRAS 19111+1048 and IRAS 19110+1045 regions are shown in Figure 11. The nearly vertical solid lines from left to right represent the ZAMS curves (for a distance of 6 kpc) reddened by $A_V = 0$, 15, and 30 mag, respectively. The slanting lines trace the reddening vectors of these ZAMS stars. We have assumed extinction values of $A_J/A_V = 0.282$, $A_H/A_V = 0.175$, and $A_{K_s}/A_V = 0.112$ from Rieke & Lebofsky (1985). All the 2MASS magnitudes as well as the ZAMS curves are in the Bessel & Brett (1988) system. In Figure 11, the triangles (IR 4 and IR 8) represent sources that are very bright in the K_s band and lie much higher than the extinction curve of an O5 star, possibly embedded or unresolved stellar objects. The asterisks represent sources of spectral type B0 or earlier lying within the radio nebulosity. The plus signs represent stars of spectral type later than B0 found within the radio nebulosity. The dots represent sources that do not lie within the radio nebulosity.

TABLE 5
Radio and Near-Infrared Sources and Their Spectral Types around IRAS 19111+1048

Radio (GMRT)		Radio (VLA)[a]		NIR (2MASS)	
Name	Spec. Type	Name	Spec. Type	Name	Spec. Type
S1	B0–O9.5	...	...	...	...
S2	B0–O9.5	...	...	...	...
S3	B0–O9.5	...	...	...	...
S4	B0–O9.5	...	...	...	...
S5	B0–O9.5	...	...	...	...
S6	O9	TFT 13	O9.5	IR 1	B0–O9
S7	O9.5–O9	...	...	...	...
S8	O9	...	...	...	...
S9	O9.5–O9	...	...	...	...
S10	B0–O9.5	...	...	...	...
S11	O7	...	...	IR 2	O9–O6
S12	O8	...	...	IR 3	B2
S13	B0.5–B0	...	...	...	...
S14	O6.5–O6	TFT 15	O6	IR 4, IR 5	X[b], O5
S15	B0–O9.5	...	...	...	...
S16	B0.5–B0	...	...	IR 6	B7–B3
S17	B0.5–B0	...	...	...	...
S18	B0–O9.5	TFT 16	B0–O9.5	...	...
S19	B0–O9.5	TFT 17	B0–O9.5	IR 7	B7–B3

[a] Work of TFT99.
[b] Either a pre–main-sequence star or compact unresolved stars (see § 5).

4. RADIATIVE TRANSFER MODELING

With the aim of extracting important physical parameters, an attempt has been made to construct radiative transfer models of the two sources IRAS 19111+1048 and IRAS 19110+1045. Although high-resolution maps in the radio and NIR indicate the presence and location of a cluster of sources, we carry out simplistic radiative transfer modeling assuming a cluster of ZAMS stars located at the center of a spherically symmetric homogeneous cloud of gas and dust. This cloud is assumed to be immersed in an isotropic radiation field (typical interstellar radiation field, ISRF). The self-consistent scheme developed by Mookerjea & Ghosh (1999) has been used here.

The physical parameters explored to get a fit to the SED are the nature of the embedded source (single or a cluster of ZAMS stars of appropriate initial mass function and mass limits), the radial density distribution law [$n(r) \propto r^{-\alpha}$, where $\alpha = 0$, 1, or 2], the relative abundances of the two constituent grain types (silicate and graphite), the total radial optical depth due to the dust, the gas-to-dust ratio by mass, and geometric details of the cloud (e.g., cavity size and outer size of the cloud). Two commonly used types of interstellar dust are explored: the type of dust grains from Draine & Lee (1984, hereafter DL84) and the dust type from Mathis et al. (1983). The observed angular sizes have been used to constrain the models.

TABLE 6
Radio and Near-Infrared Sources and Their Spectral Types around IRAS 19110+1045

Radio (GMRT)		Radio (VLA)[a]		NIR (2MASS)	
Name	Spec. Type	Name	Spec. Type	Name	Spec. Type
S21	B0–O9.5	...	...	...	...
S22[b]	B0–O9.5	...	...	K3	O6.5–O6
S23[b]	B0–O9.5	...	...	K3	O6.5–O6
S24	B0–O9.5	...	...	...	...
S25	B0.5–B0	...	...	...	...
S26	B0–O9.5	TFT 11	O9.5–O8.5	K1	...
S27	B0.5–B0	TFT 12	B0–O9.5	K2	...

[a] Work of TFT99.
[b] Radio knots that could be thermally excited by K3.

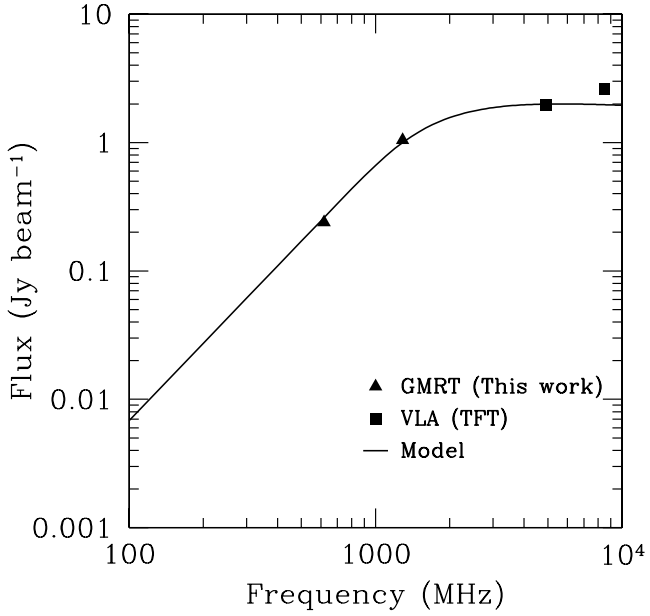

FIG. 10.—Observed (triangles and squares represent GMRT and VLA measurements, respectively) and modeled (*line*) flux densities for the core of the H II region, S14, in IRAS 19111+1048. The flux densities correspond to a beam size of 10″.

4.1. *IRAS 19111+1048*

The SED for IRAS 19111+1048 has been constructed using the flux densities obtained from the *MSX* maps, the *IRAS*-LRS data, the *IRAS*-HIRES maps, the TIFR maps, and the submillimeter (450 and 850 μm) JCMT-SCUBA maps. The SED also includes the flux densities in the *J*, *H*, and K_s bands obtained by integrating the fluxes of the 2MASS sources within a circle of diameter 3′ centered on the peak of IRAS 19111+1048. The total luminosity obtained by integrating the observed SED is $6.5 \times 10^5\ L_\odot$. We have used a cluster of 19 ZAMS OB stars, obtained from our radio measurements (first 19 sources listed in Tables 3 and 5, S20 being a nonthermal source; see § 5 for more details), as the centrally exciting sources that power this region. The total luminosity of this cluster is $8.5 \times 10^5\ L_\odot$. Modeling the SED of IRAS 19111+1048 gives a better fit for a uniform (r^0) density distribution than for the other two power laws. The outer radius of the spherical cloud is 4 pc, and the radius of the dust cavity is ~0.01 pc. The preferred dust is of the DL84 type with a radial optical depth of 0.002 at 100 μm. We have used the radius of the H II region (1.4 pc) from our 1280 MHz map to constrain the gas-to-dust ratio by mass, which is obtained as 250. This implies an underabundance of dust grains in this region. The radio continuum emission predicted by this model at 1280 MHz is 3.8 Jy, which is ~60% of the observed value. The best-fit model, along with the SED, is shown in Figure 12. The predicted emission from the model at wavelengths shorter than ~2 μm is dominated by the scattered ISRF due to dust grains in the cloud. IRAS 19111+1048 is unresolved at the *MSX* and *IRAS*-HIRES wave bands; this is consistent with the sizes obtained from the model. The expected angular sizes of IRAS 19111+1048 in the TIFR maps have been estimated from the model by convolving the predicted source size at that band with the achieved angular resolution. This is consistent with the sizes seen at 130 and 210 μm. The various parameters of the best-fit model are listed in Table 8.

4.2. *IRAS 19110+1045*

For IRAS 19110+1045, the *ISO*-SWS and *ISO*-LWS spectra from 3 to 188 μm are available. The radiative transfer modeling uses the flux densities obtained from the JCMT-SCUBA maps at the 450 and 850 μm bands to carry out radiative transfer modeling for this source. The SED also includes the total emission from 2MASS sources within the equivalent beam of *ISO*-SWS, in the *J*, *H*, and K_s bands. From our radio maps, seven radio sources have been extracted from this region (see Table 6). In our model, we have used these as the central exciting sources. The *ISO*-SWS spectrum covers the wavelength range 2–45 μm corresponding to a field of view (FOV) of 33″ × 20″. On the other hand, the *ISO*-LWS spectrum covers wavelengths longer than ~45 μm with a FOV of diameter 84″. For comparing the radiative transfer model results with the LWS and SWS data, the model results have been convolved with the appropriate beams. Consequently, we see a slight discontinuity in the SED at ~45 μm. We obtain a total luminosity of $3.3 \times 10^5\ L_\odot$ by integrating the observed SED. However, the total luminosity of the resolved stars is

TABLE 7

DETAILS OF 2MASS PSC SOURCES THAT ARE LIKELY TO BE ASSOCIATED WITH GMRT SOURCES AT 1280 MHz (SEE TABLES 5 AND 6) IN IRAS 19111+1048 AND IRAS 19110+1045 REGIONS

2MASS PSC Designation	Name[a]	α_{2000} (deg)	δ_{2000} (deg)	*J* (mag)	*H* (mag)	K_s (mag)
IRAS 19111+1048						
J19132485+1053474.....	IR 1	288.353577	10.896520	14.64 ± 0.04	13.11 ± 0.04	12.35 ± 0.05
J19132689+1054176.....	IR 3	288.362067	10.904891	15.23 ± 0.13	14.14 ± 0.13	12.83 ± 0.12
J19132692+1054269.....	IR 2	288.362188	10.907485	13.10 ± 0.03	12.03 ± 0.04	11.50 ± 0.04
J19132786+1053364.....	IR 4	288.366123	10.893447	11.87 ± 0.03	9.97 ± 0.04	7.85 ± 0.03
J19132812+1053297.....	IR 5	288.367173	10.891603	13.76 ± 0.06	11.98 ± 0.07	10.08 ± 0.05
J19132823+1054056.....	IR 6	288.367652	10.901567	16.35 ± 0.14	15.21 ± 0.09	14.95 ± 0.20
J19132895+1053560.....	IR 7	288.370642	10.898909	15.88 ± 0.09	14.96 ± 0.09	13.58 ± 0.10
IRAS 19110+1045						
J19131970+1050478.....	IR 8	288.332099	10.846624	8.14 ± 0.01	7.23 ± 0.03	6.83 ± 0.02
J19132008+1050527.....	K3	288.333708	10.847999	...	12.55 ± 0.19	11.52 ± 0.09
J19132184+1050484.....	K1	288.341025	10.846782	...	...	13.14 ± 0.14
J19132208+1050538.....	K2	288.342034	10.848284	...	...	10.54 ± 0.03

[a] Short name used in the present work (see Figs. 11, 14, and 15).

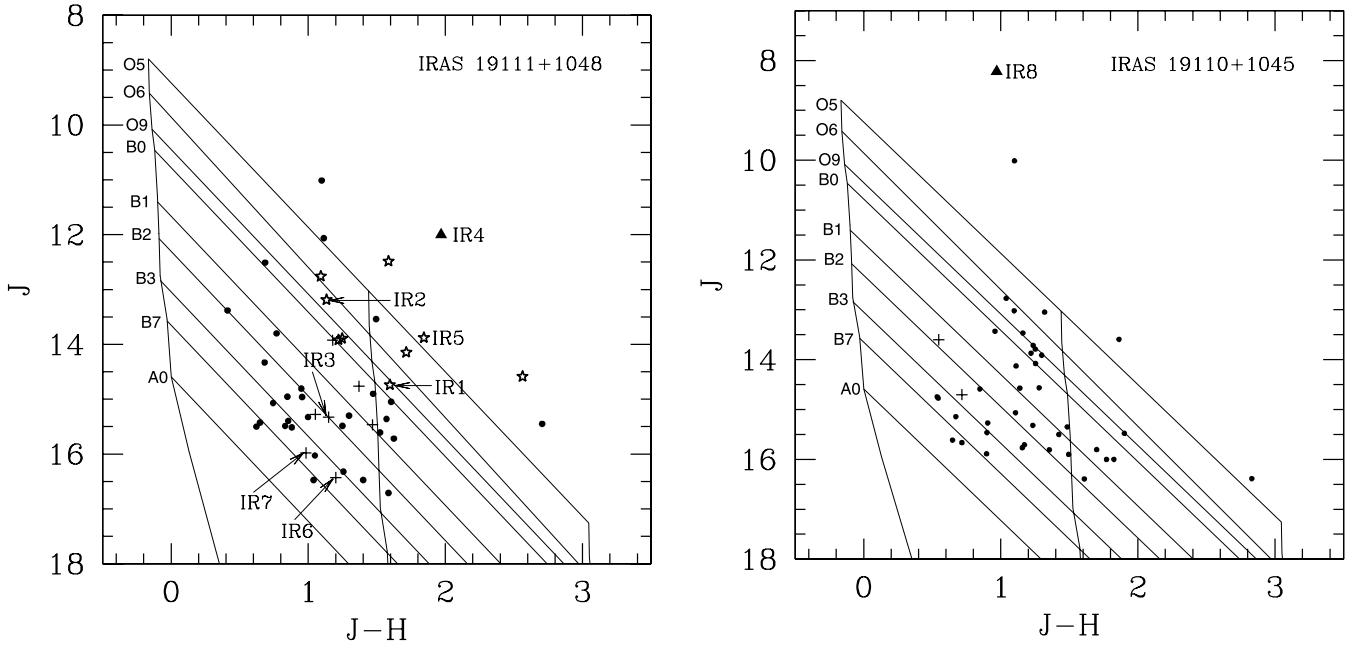

FIG. 11.—Color-magnitude diagram ($J - H$ vs. J) for sources detected in all three 2MASS bands for the region around IRAS 19111+1048 (*left*) and IRAS 19110+1045 (*right*). The nearly vertical solid lines from left to right represent the ZAMS curves reddened by $A_V = 0$, 15, and 30 mag, respectively. The slanting lines trace the reddening vectors of these ZAMS stars. The asterisks represent stars of spectral type B0 or earlier. The triangle represents an embedded source, possibly in its very early evolutionary stage or unresolved early-type stars. The plus signs are sources of spectral type later than B0 within the radio nebulosity. The dots represent selected sources not lying within the radio nebulosity. [*See the electronic edition of the Journal for a color version of this figure*.]

$1.1 \times 10^5\ L_\odot$. Guided by the composition of the observed radio spectral types as well as the luminosity obtained by integrating the SED, we carry out radiative transfer modeling. The data and the best-fit model are shown in Figure 13. The model fits the observations reasonably well. The model fitted to the observed SED best corresponds to a constant-density cloud. The radio continuum flux density predicted by the model underestimates the observed flux density by a factor of 3 at 1280 MHz but matches the flux density at 8.3 GHz (TFT99) of 0.84 Jy for a gas-to-dust ratio of 450. This gas-to-dust ratio is rather large. The radius of the H II region predicted by this model is 0.04 pc, while the radius of the region encompassing S21–S25 is found to be ~0.9–1.1 pc at 1280 MHz and 4.9 GHz. The large gas-to-dust ratio and the difference in the size of the H II region from the model and observations implies a significant difference of the true geometry of the source from the simple assumptions used in the modeling. It is likely that the medium is clumpy. The DL84 type of dust fits the data better. Table 8 lists the various parameters of the best-fit model to the SED.

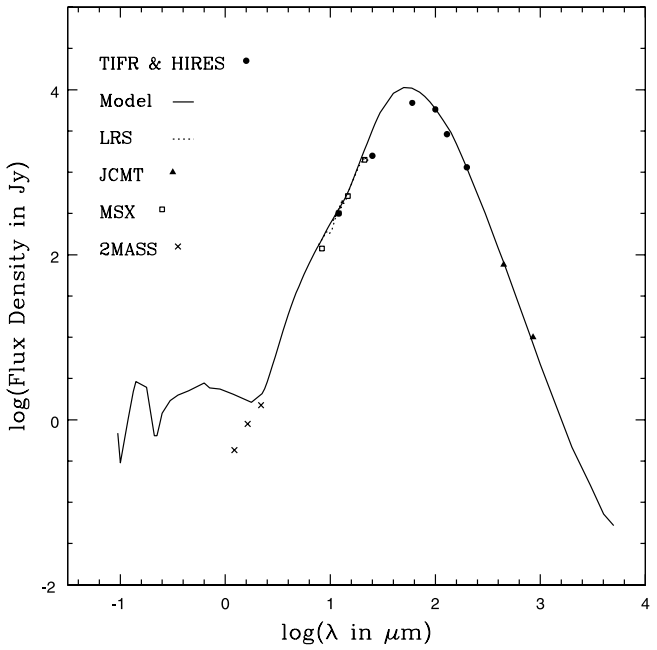

FIG. 12.—Comparison of the SED from observations and the best-fit radiative transfer model of IRAS 19111+1048. The filled circles represent the TIFR and *IRAS*-HIRES data. The dashed lines are the *IRAS*-LRS spectra. The filled triangles denote JCMT data, while the open squares represent the *MSX* data. The 2MASS data are denoted by crosses. The solid line denotes the best-fit model to the data. See text and Table 8 for details of model parameters.

5. DISCUSSION

5.1. *IRAS 19111+1048*

The far-infrared *IRAS*-HIRES, TIFR, and JCMT-SCUBA maps probe the cold dust environment around IRAS 19111+1048. The flux densities from the JCMT-SCUBA maps at 450 and 850 μm have been used to compute the mass of dust using the formulation of Hildebrand (1983) and Sandell (2000). The dust mass obtained from emission at 450 and 850 μm is ~20 $M_\odot$, while that obtained from 200 μm emission map is 18 $M_\odot$. A dust mass of 12 $M_\odot$ is obtained from the radiative transfer modeling. This compares well with the dust mass of 24 $M_\odot$ obtained by Hoare et al. (1991; scaled to our distance) from the submillimeter observations. Considering a gas-to-dust ratio of 250 by mass from the radiative transfer model (see § 4.1), we determine the gas mass in this region to be 5000 $M_\odot$.

The optical depth at 100 μm obtained from radiative transfer modeling is $\tau_{100} \sim 0.002$. This could be compared with the peak value of the optical depth at 25 μm obtained from the *IRAS*-HIRES maps, $\tau_{25} \sim 0.001$. The apparent inconsistency of the lower value of τ_{25} as compared to τ_{100} can be resolved by attributing the τ_{25} to warmer dust of smaller volume around the exciting

TABLE 8

Best-Fit Parameters of the Radiative Transfer Models for IRAS 19111+1048 and IRAS 19110+1045

Source (IRAS)	α	R_{max} (pc)	R_{min} (pc)	$r_{H\,II}$ (pc)	τ_{100}	L ($10^5\ L_\odot$)	Dust Type	Composition (Si : C)	M_{dust} ($M_\odot$)	Gas : Dust
19111+1048.....	0.0	4.0	0.01	1.5	0.002	8.5	DL84	5 : 95	12	250 : 1
19110+1045	0.0	3.5	0.01	0.04	0.10	3.3	DL84	60 : 40	450	450 : 1

sources. Faison et al. (1998) modeled the dust distribution around this source and obtained a value of $\tau_{100} = 0.01$. This discrepancy can be attributed to (1) the distance of 9.7 kpc used by them and (2) the fact that their model fits only the mid-infrared spectrum reasonably well and not the full SED.

The radio emission of this H II region indicates the extent of ionized gas. As can be seen from all the radio maps, a number of sources have been detected apart from diffuse emission. A comparison with the high-resolution maps of TFT99 at 4.9 and 8.5 GHz indicates that our source list includes all four sources detected by them. The compact sources detected by them around this ultracompact H II region are listed as sources 13, 15, 16, and 17 in their Table 1. We designate these sources as TFT 13, TFT 15, TFT 16, and TFT 17, respectively. A positional comparison of their sources and those detected by us at 1280 MHz indicates that TFT 13 can be identified with S6, TFT 15 with S14, TFT 16 with S18, and TFT 17 with S19 (Table 5). The diffuse emission corresponding to TFT 31 is emission to the northwest of S14 in our maps, which has been resolved into multiple sources here. A comparison between the 1280 and 610 MHz maps shows that many sources that have been detected in the former are not resolved in the latter.

For the point source S20, we find that the flux density at 610 MHz is higher than the flux density at the 1280 MHz band, corresponding to a power-law spectral index of -0.6. This indicates a nonthermal nature of the radio emission. Assuming this spectral index, the expected flux densities at 4.9 and 8.5 GHz are 8.6 and 6.2 mJy, respectively. The absence of this source from the maps of TFT99 is consistent with the lowest peak values of the compact sources listed in their Table 1: 17 mJy beam^{-1} at 4.9 GHz and 24 mJy beam^{-1} at 8.5 GHz. Although S20 is in the vicinity of IRAS 19111+1048, it is unlikely to be associated with IRAS 19111+1048, and consequently we do not consider S20 as a part of this H II region for further analysis. In the 325 MHz image, we do not see this source due to the resolution effect, although an extension corresponding to this source can be seen.

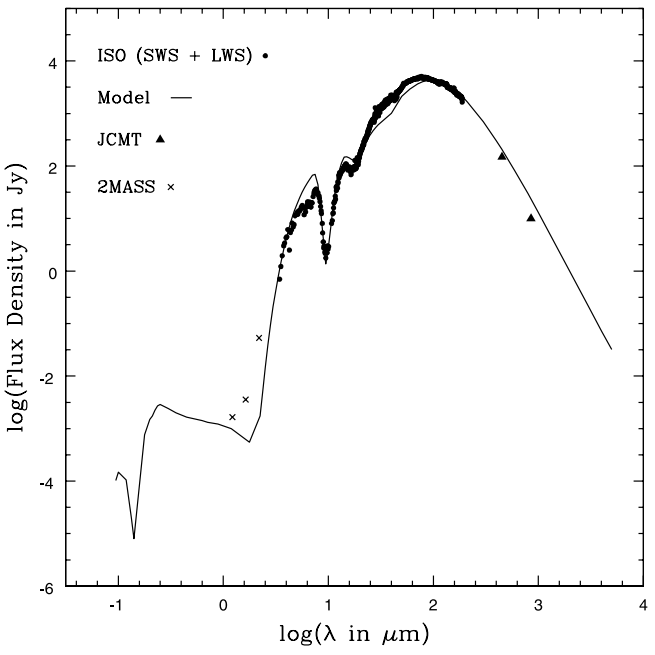

Fig. 13.—Comparison of the SED from observations and the best-fit radiative transfer model of IRAS 19110+1045 for *ISO* data. The filled circles represent the *ISO* SWS and LWS data, the filled triangles represent JCMT data, and the crosses represent the 2MASS data. The solid line denotes the best-fit model to the data. See Table 8 for details of model parameters.

Using the 19 radio sources, we find the slope of the initial mass function [$\xi(m) \propto m^{-a}$] in this star-forming region to be $a = 5.3 \pm 0.5$ in the mass range $14 < m/M_\odot < 33$. The initial mass function is quite steep, implying a scarcity of massive and luminous stars in this region. Such a steep power law of the initial mass function is characteristic of young star-forming regions. For example, Ghosh et al. (1989) obtained $a = 6$ and 3 for the regions W31 and W33, respectively, for $20 < m/M_\odot < 35$ using a similar analysis.

We now identify the NIR counterparts of these radio sources using the position information ($<2\farcs5$; resolution of 1280 MHz map) from the 2MASS NIR images and catalogs. We designate these NIR sources as IR 1, IR 2, . . . , IR 7 (Table 7). The 1280 MHz radio contours are plotted over the 2MASS K_s-band image, shown in Figure 14. Some of the radio sources with their possible ionization sources from the NIR (position and color) are also compared in Table 5. Six sources have been identified, of which the spectral types deduced from radio emission of the three sources S6, S11, and S14 agree quite well with the spectral types obtained from NIR measurements. We have also checked for a positional match of the radio sources with sources detected in the H and K_s bands or only in the K_s band. We find only one such match for S4, which is detected in only the K_s band (magnitude $\sim$14.1).

The compact H II source S14 is deduced to be of spectral type O6 from the integrated radio emission. There are two NIR objects, IR 4 and IR 5, within the S14 region obtained from the NIR catalog and images. IR 4 is at the peak of the radio emission and matches the OH maser position ($\alpha_{2000} = 19^h13^m27\fs8$, $\delta_{2000} = +10^\circ53'37''$) obtained by Argon et al. (2000). IR 4 is very bright in the K_s band (magnitude $\sim$7.9) and appears to be of a spectral type much earlier than O5, as indicated by a triangle in the CM diagram. It could be an embedded pre–main-sequence star, or it is likely to comprise two or more unresolved early-type stars. Hunter et al. (1997) detected two sources of CO bipolar outflow, one of which is at the location of the radio peak IR 4. Considering the facts that (1) IR 4 is coincident with the OH maser position, (2) it is the source of a bipolar outflow, and (3) it has a large infrared excess ($J - K \sim 4.0$), it is likely that this source could be an embedded pre–main-sequence object. The ionization of gas could also be attributed to IR 5, which according to our CM diagram is of stellar type O5. It is interesting to note that although the source S14 peaks at the position of an *IRAS* source, the radio morphology in all the three GMRT bands shows a north-south extension, indicating that perhaps this is not a single compact core but rather

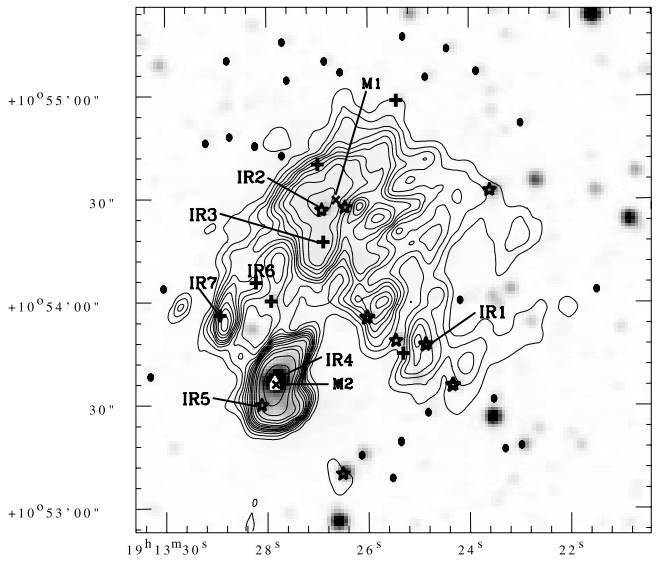

FIG. 14.—Contours of high-resolution radio continuum emission at 1280 MHz laid over the gray-scale 2MASS K_s-band image for the region around IRAS 19111+1048. The labeled axes are in J2000.0 coordinates. Various NIR and *MSX* sources are marked. The crosses represent *MSX* sources. The description of the other symbols is the same as given in Fig. 11. [*See the electronic edition of the Journal for a color version of this figure.*]

has more than one H II clump. This is also clearly evident from the maps of TFT99. Kraemer et al. (2003) find that the IRAS 19111+1048 core consists of two compact mid-infrared (12.5 and 20.6 μm) components. If we consider sources only detected in the K_s band within the S14 region, we find that there are four more NIR sources detected. It thus appears that the source S14 has a compact embedded cluster and is perhaps a conglomeration of H II clumps, the brightest one at the position of S14.

For the sources S6, S11, and S14, the spectral types obtained from radio measurements and NIR colors agree very well. However, the agreement is not good for S16, S19, and S12. S16 and S19 are found to be of spectral types B0.5–B0 and B0–O9.5, respectively. They are associated with IR 6 and IR 7, respectively, which are of spectral type B7–B3 obtained from the NIR CM diagram. Most probably, IR 6 and IR 7 are reddened main-sequence foreground sources based on their position in the CM diagram. For S12 as well, we find that the radio and NIR spectral types do not match. While the radio spectral type of the ZAMS star is O8, the NIR counterpart is of spectral type B2. These three cases could be spurious associations. This number of spurious associations can be compared with the estimated number of chance associations of 1.3 obtained by considering the density of NIR sources (detected in H and K_s bands) and the search radius of $\sim$2.″5 of the 19 radio sources.

From the NIR CM diagram, we see that most of the ZAMS stars within the radio nebulosity have extinction values corresponding to $A_V \sim 10-35$ mag. This is quite consistent with the extinction values obtained ($A_V = 10-30$) by Hoare et al. (1991). Lumsden & Puxley (1996) obtained $A_V \sim 24$ from Brγ imaging and radio continuum observations for this source.

Although the radio and NIR K_s-band images indicate a positional match for some radio and NIR sources (with consistent spectral types), there are a number of radio sources that do not have a NIR counterpart. The radio spectral types indicate that these are bright sources that ought to have been detected in the NIR. Their absence gives rise to two possibilities: (1) the radio sources are high-density ionized clumps with no centrally exciting star, or (2) the medium is clumpy with dense distributions of $A_V > 30$, while the average visual extinction is lower ($A_V \sim 15$). Next, we show that the first scenario of high-density clumps being ionized by ZAMS stars located away from them can be ruled out. For instance, S13 does not have a NIR counterpart. An estimation of the Lyman continuum photons reaching S13 from its neighbor S14 (the brightest source in this region; see Fig. 6) due to geometric factors shows that in the absence of any intervening medium, the expected luminosity is only 5% of its observed luminosity. Hence, it is more likely that the second scenario is responsible for the nondetection of the NIR counterparts. A high-resolution mapping of molecular species probing the cold and dense gas over a large region ($\sim$1.′5) around this source is required to better our understanding of the physical picture of this region. The radio morphology toward the northeast of the extended radio emission indicates the steepness of the gradient of the radio emission. This could be due to the restriction of the ionized region by molecular gas, as seen in other regions such as S201 (Ojha et al. 2004a) and NGC 7538 (Ojha et al. 2004b).

We have also cross-correlated the *MSX* PSC sources with those from the 2MASS PSC that lie within the radio nebulosity. There are two such *MSX* PSC sources, G045.1331+00.1436 and G045.1221+00.1323 (hereafter M1 and M2, respectively; listed in Table 9 and shown in Fig. 14). While M1 is close to IR 2 ($\sim$5″), M2 coincides with IR 4. From the 2MASS-*MSX* color-color diagram (F_{21}/F_8 vs. F_8/F_K; Lumsden et al. 2002), we find that these sources lie in the region generally covered by compact H II regions. We can therefore conclude that these are young stars associated with the cluster.

5.2. *IRAS 19110+1045*

The SED of IRAS 19110+1045 shows a very strong silicate feature at 10 μm. From radiative transfer modeling, we get a higher composition of silicate (60%) grains. The optical depth at 100 μm from the model is 0.1. This is consistent with the value of $\tau_{100} = 0.085$ obtained by Faison et al. (1998) using their spherically symmetric dust shell model. A gas-to-dust ratio by mass of 450 is obtained for consistency with radio observations. The dust mass corresponding to the above model is 450 $M_\odot$. On the other hand, the 130 μm emission map gives a dust mass of 13 $M_\odot$. However, based on the submillimeter (JCMT-SCUBA) maps, we obtained a cold dust mass of $\sim$30 $M_\odot$, implying a gas mass of 1.3×10^4 $M_\odot$.

From the radio image at the 1280 MHz band, we see that this H II region consists of seven radio sources, of which S21–S25 form a complex that is separated from the two compact sources S26 and S27. This is consistent with what TFT99 obtained in their high-resolution VLA mapping of this source at 4.9 and 8.5 GHz. While S26 and S27 can be identified with TFT 11 and TFT 12, respectively, TFT 30 is resolved into S21–S25. At 610 MHz, these sources are unresolved. The image at 325 MHz shows a single source at this frequency. The ZAMS spectral types obtained from the radio flux densities from our maps and the maps of TFT99 are consistent (Table 6).

A comparison of the 1280 MHz radio emission with the NIR K_s band emission is shown in Figure 15. The two compact radio sources, S26 and S27, do not have any NIR counterparts that are detected in all the three JHK_s bands. We, however, note that there are two sources, designated as K1 and K2, detected only in the K_s band, which match (<2.″5) with S26 and S27, respectively. It is likely that these objects are deeply embedded. Garay et al. (1986) have used the H76α line and continuum emission to show

TABLE 9

DETAILS OF *MSX* PSC SOURCES WITHIN THE RADIO NEBULOSITY OF IRAS 19111+1048 AND IRAS 19110+1045 REGIONS

MSX PSC Designation	Name[a]	α_{2000} (deg)	δ_{2000} (deg)	F_8 (Jy)	F_{12} (Jy)	F_{14} (Jy)	F_{21} (Jy)
G045.1331+00.1436	M1	288.3610	10.9083	4.7 ± 0.2	8.3 ± 0.9	32.1 ± 2.0	57.6 ± 3.5
G045.1221+00.1323	M2	288.3660	10.8933	87.5 ± 3.6	296.4 ± 14.8	455.7 ± 27.8	1061.7 ± 63.7
G045.0711+00.1325.....	M3	288.3417	10.8482	20.3 ± 0.8	53.8 ± 2.7	119.3 ± 7.3	256.0 ± 15.4
G045.0668+00.1372	M4	288.3354	10.8466	3.6 ± 0.1	9.0 ± 0.5	11.0 ± 0.7	35.8 ± 2.2

[a] Short name used in the present work (see Figs. 14 and 15).

that the structure of G45.07+0.13 (positional match with S27) suggests the existence of an ionized ring. According to them, this ionized toroidal structure is likely to correspond to the inner ionized walls of a disk surrounding an inner massive star. This could explain the 2MASS NIR detection only in the K_s band. Since S26 also has compact radio emission and a NIR counterpart detected only in the K_s band, it is likely that it is also in a similar stage of evolution. Kraemer et al. (2003) have studied this source as a part of their Galactic Ring Survey in the mid-infrared (12.5 and 20.6 μm), and they find three mid-infrared compact sources, one located at the position of S26 and two close (2″) compact sources near S27; the brighter of them matches in position with S27. The OH maser position (Argon et al. 2000) and CO bipolar outflow detected by Hunter et al. (1997) is at the position of S27. Hanson et al. (2002) have reported that this source is heavily reddened in the K-band spectrum ($A_K = 8$), and no emission is seen in the H-band spectrum.

Considering the radio nebulosity encompassing S21–S25, we find that there are four NIR sources within it. IR 8 is very bright in the J (8.1) as well as the K_s (6.8) band. Although it lies much higher than the ZAMS curves in the CM diagram, it does not have an associated maser or outflows (as in the case of IR 4). It is therefore likely to be a foreground source rather than an embedded early-type star associated with this source. We attribute the radio emission to another source, designated K3, detected only in the H and K_s bands. K3 is of ZAMS spectral type O6.5–O6 from the ($H - K$ vs. K) CM diagram. The other two sources within the radio nebulosity are of later spectral types (later than B1). Since K3 does not match in position with any of the radio sources, we explore whether S21, . . . , S25 are clumps of dense gas externally excited by K3. For this, the role of geometric dilution is considered as discussed for S13 in § 5.1. We find that only S22 and S24 can barely be excited by K3, while S21, S23, and S25 cannot be ionized by K3.

In this H II region, we find that there are two *MSX* PSC sources, G045.0668+00.1372 and G045.0711+00.1325 (designated M3 and M4, respectively; listed in Table 9 and shown in Fig. 15), within the radio nebulosity. M4 is close to K1 and K2, while M3 can be associated with K3. As in the case of IRAS 19111+1048, we obtain the 2MASS-*MSX* colors (F_{21}/F_8 and F_8/F_K; Lumsden et al. 2002) and observe that M3 and M4 lie in the general region covered by compact H II regions.

5.3. *Comparison of Properties of IRAS 19111+1048 and IRAS 19110+1045*

The properties of the two neighboring star-forming regions as obtained from infrared and radio studies have been compared here. The physical extent of ionized gas around IRAS 19111+1048 (2.8 pc) is larger than that of its neighbor, IRAS 19110+1045 (1.3 pc). A comparison of the optical depth of the cold dust, τ_{100}, obtained from the radiative transfer model indicates that the dust around IRAS 19111+1048 is optically thin ($\tau_{100} \sim 0.002$) compared to that around IRAS 19110+1045 ($\tau_{100} \sim 0.1$). The ratios of total luminosity to the cloud mass of IRAS 19111+1048 and IRAS 19110+1045 are 170 and 24 $L_\odot\ M_\odot^{-1}$, respectively. The lower value of L/M of IRAS 19110+1045 indicates that it is younger than its neighboring star-forming region. The near-infrared data as well as high-resolution radio measurements indicate that IRAS 19111+1048 has a larger number of ZAMS stars energizing compact and evolved H II regions. On the other hand, IRAS 19110+1045 shows the presence of seven radio sources. The NIR counterparts of two of the compact H II sources (S26 and S27) have been detected only in the K_s band, indicating that they are deeply embedded in dust. In view of the above, viz., the lower L/M ratio of IRAS 19110+1045, its smaller extent of ionized gas, fewer ZAMS stars, and the presence of compact H II regions harboring deeply embedded stars, IRAS 19110+1045 is likely to be younger than IRAS 19111+1048, as suggested by others (Hunter et al. 1997; Kraemer et al. 2003).

6. SUMMARY

The star-forming regions associated with IRAS 19111+1048 and IRAS 19110+1045 have been studied at infrared (near, mid-, and far-), submillimeter, as well as low-frequency radio wave bands. The dust environment of these regions is probed using data from the TIFR balloon-borne telescope (130 and 200 μm), *MSX*, *IRAS*-HIRES, JCMT-SCUBA, and *ISO*. Using the 2MASS PSC,

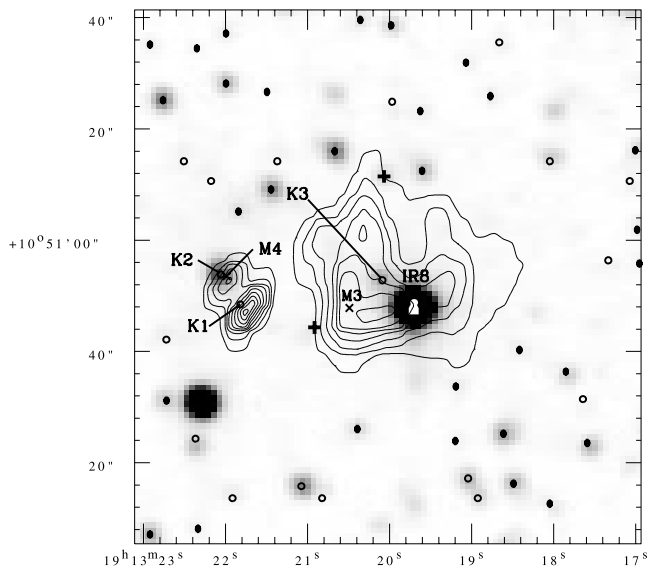

FIG. 15.—Same as in Fig. 14, but for the region around IRAS 19110+1045. The open circles indicate the sources detected only in H and K_s bands or only in the K_s band. [*See the electronic edition of the Journal for a color version of this figure.*]

the NIR sources in these regions have been extracted and studied using color-magnitude (CM) diagrams. The distribution of ionized gas has been obtained using high angular resolution radio maps from GMRT (325, 610, and 1280 MHz). The radio morphology indicates the presence of a highly inhomogeneous medium. Twenty compact radio sources have been extracted from IRAS 19111+1048, and seven from IRAS 19110+1045. One of the compact sources (S20) is found to be of nonthermal nature based on its spectral index ($\alpha = -0.6$). The rest of the sources in the IRAS 19111+1048 region are of spectral type earlier than B0.5. Based on these sources, the power-law index of the initial mass function has been found to be 5.3 ± 0.5 for the mass range $14 < m/M_{\odot} < 33$. The compact source S14 is located at the position of this *IRAS* source. The near-infrared (NIR) source coincident with the *IRAS* peak is likely to be an embedded pre–main-sequence star due to its large infrared excess as well as the presence of an OH maser and CO bipolar outflow here. The electron temperature and emission measure of S14 using results from GMRT (our work) and VLA (TFT99) measurements are determined to be 8346 ± 1511 K and $8.8 \pm 0.7 \times 10^6$ cm^{-6} pc, respectively. A comparison of NIR and radio images has been carried out to identify the exciting sources and their nature. The spectral types determined from NIR and radio measurements are found to match very well for a good fraction of radio sources having NIR counterparts. The radio and infrared morphology of IRAS 19110+1045 indicates that the extent of dust as well as ionized gas is relatively smaller than that of IRAS 19111+1048. The two compact radio sources, S26 and S27, have been detected only in the K_s band, indicating that these are deeply embedded. Self-consistent radiative transfer modeling has been carried out with spherical gas/dust clouds for both the *IRAS* sources, using a cluster of OB stars as determined from the radio maps. A constant radial density distribution [$n(r) \propto r^0$] is preferred. The geometric details of the gas/dust clouds, the dust composition, optical depths, etc., have been quantified by the models. A comparative study of the infrared and radio properties of IRAS 19110+1045 and IRAS 19111+1048 supports the younger nature of the former, consistent with earlier studies.

We thank the anonymous referee for comments and suggestions that improved the paper. It is a pleasure to thank several members of the Infrared Astronomy Group of TIFR for their support during the balloon flight campaigns. All members of the TIFR Balloon Facility, Hyderabad, are thanked for their technical support for the flight. We thank the staff of the GMRT, who have made the radio observations possible. GMRT is run by the National Centre for Radio Astrophysics of the Tata Institute of Fundamental Research. We thank IPAC, Caltech, for providing us the HIRES-processed *IRAS* products.

REFERENCES

Altenhoff, W. J., Downes, D., Pauls, T., & Schraml, J. 1979, A&AS, 35, 23
Araya, E., Hofner, P., Churchwell, E., & Kurtz, S. 2002, ApJS, 138, 63
Argon, A. L., Reid, M. J., & Menten, K. M. 2000, ApJS, 129, 159
Aumann, H. H., Fowler, J. W., & Melnyk, M. 1990, AJ, 99, 1674
Bessel, M. S., & Brett, J. M. 1988, PASP, 100, 1134
Clegg, P. E., et al. 1996, A&A, 315, L38
Darbon, S., Zavagno, A., Perrin, J.-M, Savine, C., Ducci, V., & Sivan, J.-P. 2000, A&A, 364, 723
de Graauw, Th., et al. 1996, A&A, 315, L49
Draine, B. T., & Lee, H. M. 1984, ApJ, 285, 89 (DL84)
Egan, M. P., et al. 2003, MSX6C Infrared Point Source Catalog (AFRL-VS-TR-2003-1589; Bedford: AFCRL)
Faison, M., Churchwell, E., Hofner, P., Hackwell, J., Lynch, D. K., & Russell, R. W. 1998, ApJ, 500, 280
Fish, V. L., Reid, M. J., Wilner, D. J., & Churchwell, E. 2003, ApJ, 587, 701
Frieswijk, W. F., Shipman, R. F., & Lahuis, F. 2004, *ISO* Technical Note 12 (Villafranca: VILSPA), http://pma.iso.vilspa.esa.es:8080/hpdp/technical_reports/technote12.pdf
Garay, G., Rodriguez, L. F., & van Gorkom, J. H. 1986, ApJ, 309, 553
Genzel, R., & Downes, D. 1977, A&AS, 30, 145
Ghosh, S. K., Iyengar, K. V. K., Rengarajan, S. N., Tandon, S. N., Verma, R. P., & Daniel, R. R. 1988, ApJ, 330, 928
Ghosh, S. K., Iyengar, K. V. K., Rengarajan, T. N., Tandon, S. N., Verma, R. P., Daniel, R. R., & Ho, P. T. P. 1989, ApJ, 347, 338
Ghosh, S. K., & Ojha, D. K. 2002, A&A, 388, 326
Goss, W. M., Lockhart, I. A., Fomalont, E. B., & Hardebeck, E. G. 1973, ApJ, 183, 843
Gull, S. F., & Daniell, G. J. 1978, Nature, 272, 686
Hanson, M. M., Luhman, K. L., & Rieke, G. H. 2002, ApJS, 138, 35
Haslam, C. G. T., Stoffel, H., Salter, C. J., & Wilson, W. E. 1982, A&AS, 47, 1
Hildebrand, R. H. 1983, QJRAS, 24, 267
Hoare, M. G., Roche, P. F., & Glencross, W. M. 1991, MNRAS, 251, 584
Hunter, T. R., Phillips, T. G., & Menten, K. M. 1997, ApJ, 478, 283
Israel, F. P. 1982, ApJ, 255, 475
Kraemer, K. E., et al. 2003, ApJ, 588, 918
Lloyd, C., Lerate, M. R., & Grundy, T. W. 2003, *ISO* Technical Note 17 (Villafranca: VILSPA), http://pma.iso.vilspa.esa.es:8080/hpdp/technical_reports/technote17.html
Lumsden, S. L., Hoare, M. G., Oudmaijer, R. D., & Richards, D. 2002, MNRAS, 336, 621
Lumsden, S. L., & Puxley, P. J. 1996, MNRAS, 281, 493
Mathis, J. S., Mezger, P. G., & Panagia, N. 1983, A&A, 128, 212
Matthews, H. E., Goss, W. M., Winnberg, A., & Habing, H. J. 1977, A&A, 61, 261
Mezger, P. G., & Henderson, A. P. 1967, ApJ, 147, 471
Mookerjea, B., & Ghosh, S. K. 1999, J. Astrophys. Astron., 20, 1
Naik, M. V., D'Costa, S. L., Ghosh, S. K., Mookerjea, B., Ojha, D. K., & Verma, R. P. 2000, PASP, 112, 273
Ojha, D. K., Ghosh, S. K., Kulkarni, V. K., Testi, L., Verma, R. P., & Vig, S. 2004a, A&A, 415, 1039
Ojha, D. K., et al. 2004b, ApJ, 616, 1042
Olnon, F. M., et al. 1986, A&AS, 65, 607
Panagia, N. 1973, AJ, 78, 929
Pankonin, V., Churchwell, E., Watson, C., & Bieging, J. H. 2001, ApJ, 558, 194
Price, S. D., Egan, M. P., Carey, S. J., Mizuno, D. R., & Kuchar, T. A. 2001, AJ, 121, 2819
Rieke, G. H., & Lebofsky, M. J. 1985, ApJ, 288, 618
Sandell, G. 2000, A&A, 358, 242
Sanders, D. B., Clemens, D. B., Scoville, N. Z., & Solomon, P. M. 1986, ApJS, 60, 1
Schraml, J., & Mezger, P. G. 1969, ApJ, 156, 269
Shepherd, D. 2005, in IAU Symp. 227, Massive Star Birth: A Crossroads of Astrophysics, ed. R. Cesaroni et al. (Cambridge: Cambridge Univ. Press), 237
Simon, R., Jackson, J. M., Clemens, D. P., & Bania, T. M. 2001, ApJ, 551, 747
Sloan, G. C., Kraemer, K. E., Price, S. D., & Shipman, R. F. 2003, ApJS, 147, 379
Swarup, G., Ananthakrishnan, S., Kapahi, V. K., Rao, A. P., Subrahmanya, C. R., & Kulkarni, V. K. 1991, Curr. Sci., 60, 95
Testi, L., Felli, M., & Taylor, G. B. 1999, A&AS, 138, 71 (TFT99)
Wood, D. O. S., & Churchwell, E. 1989, ApJS, 69, 831